**ChemPhotoChem**

Research Articles
doi.org/10.1002/cptc.202100248

Check for updates

Europe
European Chemical
Societies Publishing

www.chemphotochem.org

# High Refractive Index Dielectric Nanoparticles for Optically-Enhanced Activity of Water-Splitting Photoanodes

Luc Driencourt,[a, b, c] Benjamin Gallinet,*[a] Catherine E. Housecroft,[b] Sören Fricke,[a] and Edwin C. Constable*[b]

Metal oxide semiconductors have shown considerable potential for photoelectrochemical water-splitting. However, no ideal material has emerged which benefit from both an attractive sunlight absorption and efficient charge transport properties. In this work, we show that decorating photoanodes with high refractive index nanoparticles such as amorphous titania can result in reduced reflection losses at the electrolyte/photoanode interface, thereby increasing the performances under illumination from the electrolyte side. A proof of concept is obtained for a bismuth vanadate photoanode including a surface catalyst and a hematite photoanode. The photocurrent density and external quantum efficiency are improved by up to 10% upon nanoparticle decoration, quantitatively matching the decrease in reflectance. Simulations show that a similar enhancement happens when a thick bismuth vanadate photoanode with optimal charge transport properties is considered, thereby suggesting that this strategy can improve photoanodes suffering from high reflection losses regardless of the bare sample performance.

## Introduction

Solar water-splitting with photoelectrochemical (PEC) cells has the potential of being competitive compared to the reforming of fossil fuels for hydrogen production.[1] Recently, intensive efforts have been made with the goal of developing high performance, inexpensive materials from which photoelectrodes can be fabricated with a lifetime of several years. Metal oxide semiconductors have been intensively investigated because of their low cost and relatively good stability to photocorrosion in aqueous conditions.[2–4] Among photoanode materials, bismuth vanadate ($BiVO_4$) has demonstrated the highest performances as a bare material[5,6] or combined with highly nanostructured host scaffolds.[7,8] Strategies involving doping during synthesis[9–11] or with post treatment[12–14] and development of high performance surface catalysts[15,16] were demonstrated to be effective in improving the charge transport properties, charge transfer efficiency and stability against photocorrosion of $BiVO_4$ electrodes. For a high number of photogenerated charge carriers to participate in the water oxidation reaction, most of the light should be absorbed in the space charge region (SCR) where band bending enables generated electrons to be separated from holes, or close to the SCR with respect to the charge carriers diffusion length.[4,17, 18]

Using plasmonic nanoparticles or nanostructures has been demonstrated to be helpful for increasing the quantity of light absorbed close to the semiconductor/electrolyte interface[19–21]. The ability of plasmonic nanostructures to confine the electromagnetic field over small distances can result in field hot-spots near the nanoparticles.[22] Gold is the most robust plasmonic material used for water-splitting (stable in aqueous conditions, does not oxidize easily at high temperature in contrast to silver and aluminium). However, the natural plasmon resonance of gold nanoparticles is at higher wavelengths than the high absorption region of most metal oxides used for water-splitting.[23,24] As a consequence, plasmonic enhancements with gold are not optimal compared to other plasmonic materials, such as silver[25,26] or aluminium.[27] On the other hand, optical losses associated with plasmonic nanoparticles on resonance or due to interband transitions are ultimately detrimental to the solar-to-hydrogen efficiency of the whole device.[28] When measurements with a sacrificial hole scavenger in the electrolyte were used to isolate the optical contributions,[29,30] plasmonic effects originating from metallic nanoparticles deposited on the surface were found to be more effective when the light was incident from the substrate side (back illumination).[25,31,32] However, materials such as hematite are known to exhibit higher performances when light is incident from the electrolyte side (front illumination), because of the limiting hole transport with respect to electron transport.[33,34] In addition, numerous reported devices performing bias-free

[a] L. Driencourt, Dr. B. Gallinet, Dr. S. Fricke
CSEM Muttenz
Tramstrasse 99, 4132 Muttenz (Switzerland)
E-mail: bgt@csem.ch
[b] L. Driencourt, Prof. Dr. C. E. Housecroft, Prof. Dr. E. C. Constable
Department of Chemistry
University of Basel
BPR1096, Mattenstrasse 24a
4058 Basel (Switzerland)
E-mail: edwin.constable@unibas.ch
[c] L. Driencourt
Swiss Nanoscience Institute
Klingelbergstrasse 82, 4056 Basel (Switzerland)

**ChemPhotoChem**

Research Articles
doi.org/10.1002/cptc.202100248

**Chemistry
Europe**
European Chemical
Societies Publishing

water-splitting include a $BiVO_4$[8,35–41] or $\alpha$-$Fe_2O_3$[40,42–44] photo-anode working under front illumination. This is mandatory in the case of monolithic devices. A major drawback of the front illumination configuration is the high reflection losses at the electrolyte/metal oxide interface due to the high refractive index of metal oxide semiconductors compared to water.[45–47]

In this work, we study the benefit of depositing amorphous titania nanoparticles ($TiO_2$), which have no intrinsic photo-catalytic activity, on the surface of two different photoanodes: (i) molybdenum-doped bismuth vanadate photoanodes including a cobalt-phosphate oxygen evolution reaction (OER) surface catalyst (Mo:$BiVO_4$/Co—Pi) and (ii) hematite photoanodes ($\alpha$-$Fe_2O_3$). We show that such a decoration with high refractive index nanoparticles can improve the PEC performances under front illumination. $TiO_2$ has the advantage of being highly resistant in aqueous conditions, inducing very low optical losses and being inexpensive. Inkjet printing is used as deposition technique to demonstrate the scalability of the approach. Our analysis reveals that the nanoparticles enhance optically the photocurrent by directing the incident light toward the semiconductor material and decreasing the reflectance. We demonstrate that this strategy increases the amount of light reaching the Mo:$BiVO_4$ layer in a similar way to anti-reflective (AR) layers, with the benefit that the semi-conductor/electrolyte interface can remain photochemically active. We finally analyze the contribution of the nanoparticles using both back and front illumination and discuss how it compares to plasmonic nanoparticles.

## Results and Discussion

### Fabrication and PEC performances of Mo:$BiVO_4$/Co-Pi/$TiO_2$ photoanodes

Figure 1a shows the fabrication process of Mo:$BiVO_4$/Co—Pi/$TiO_2$ photoelectrodes, and Figures 1b–c show scanning electron microscope (SEM) images of the final sample. The fabrication process of Mo:$BiVO_4$ with 7% Mo doping yields a dense film of about 75 nm thickness. A cobalt-phosphate (Co—Pi) oxygen evolution reaction (OER) surface catalyst is deposited to improve the interfacial hole transfer,[15,16,48] and the resulting morphology is a uniform Co—Pi layer of about 20 nm thickness. An up-scalable inkjet printing technique is used for subsequent deposition of $TiO_2$ nanoparticles with an average diameter of 300 nm. The nanoparticles surface coverage (ratio of the surface covered with nanoparticles when seen from top) is about 40% in the final sample (Figure 1b). Moreover, Figure 1c shows that the contact area between the $TiO_2$ nanospheres and the underneath layers is small because of the spherical shape of the nanoparticles. Figure 1d shows schematically the beneficial effect of the $TiO_2$ nanoparticles for increasing the amount of light reaching the Mo:$BiVO_4$ layer. This will be discussed in detail in the section " Analysis of the enhancement mechanism". $TiO_2$ nanoparticles were also deposited on hematite ($\alpha$-$Fe_2O_3$) photoanodes (Figure 1e) in order to study the applicability of the method to other semiconductor

materials (section "$TiO_2$ nanoparticles deposited on $\alpha$-$Fe_2O_3$ photoanodes").

The beneficial effect of the $TiO_2$ nanoparticles was inves-tigated by measuring the photocurrent density curve under applied bias and the external quantum efficiency (EQE) at 1.23 V vs RHE in a 0.2 M $K_2HPO_4$/$KH_2PO_4$ potassium phosphate buffer (KPi, pH = 7.4). Figure 2a shows the photocurrent den-sity-voltage curves of Mo:$BiVO_4$/Co—Pi and Mo:$BiVO_4$/Co—Pi/$TiO_2$ under front illumination. It can be seen that the photocurrent density is increased by about 10% after $TiO_2$ nanoparticles deposition. At 1.23 V vs RHE the photocurrent density of the Mo:$BiVO_4$/Co—Pi/$TiO_2$ sample reaches 1.80 mA/cm². This value is similar to previously reported ultrathin $BiVO_4$/Co—Pi photoanodes[45,49] and represents 58% of the maximal achiev-able photocurrent density for a 75 nm $BiVO_4$ layer (from the calculated absorption in water by assuming 100% internal quantum efficiency). The applicability of this strategy to thick $BiVO_4$ electrodes with optimal charge transport properties is discussed in section "Analysis of the enhancement mechanism". EQE measurements under front illumination show a similar increase of about 10% (Figure 2b), almost constant through the whole spectral range. In contrast, the EQE spectra and the photocurrent densities (Figure S1) of Mo:$BiVO_4$/Co—Pi/$TiO_2$ and Mo:$BiVO_4$/Co—Pi are similar under back illumination.

Several effects could explain the enhanced performances after decoration with amorphous $TiO_2$ nanoparticles: (i) An additional photocurrent coming from the photocatalytic prop-erties of $TiO_2$. (ii) Improved hole injection and/or charge separation in Mo:$BiVO_4$ after decoration. (iii) An improved light absorption in the active material resulting from the light/nanoparticles interaction. The photocurrent density of $TiO_2$ nanoparticles deposited on FTO with a similar surface coverage was measured to investigate the first possibility (Figure S2). It was found to be ∼ 10 000 times smaller than the enhancement observed in Figure 2a. Next, it has been previously reported that a thin amorphous $TiO_2$ overlayer deposited on a $BiVO_4$/$\alpha$-$Fe_2O_3$ photoanode can result in improved performances[50–52]. In most cases, this was attributed to reduced surface recombina-tions due to surface defects passivation.[50,52] It was also suggested that the thin amorphous $TiO_2$ layer could increase the band bending in the active material.[51] In our case, the regions where the nanoparticles are in contact with the underneath layers represent only ∼3% of the total electrode surface (estimated from Figure 1c). Moreover, the nanoparticles are not in contact with $BiVO_4$ but deposited on the Co—Pi OER layer. Finally, none of these two effects can explain the significant differences observed under back and front illumina-tion. The third possibility was studied by analyzing the experimental results with our recently developed method that models optical enhancement in water-splitting photoelectro-des, following the procedure described in Ref. [32]. The light intensity distribution in periodic geometries describing realisti-cally fabricated Mo:$BiVO_4$/Co—Pi/$TiO_2$ and Mo:$BiVO_4$/Co—Pi sam-ples was first calculated with electromagnetic simulations (we showed in our recent work that periodic boundary conditions can be used to describe precisely randomly distributed plasmonic nanoparticles on $BiVO_4$.[32]) The model was then
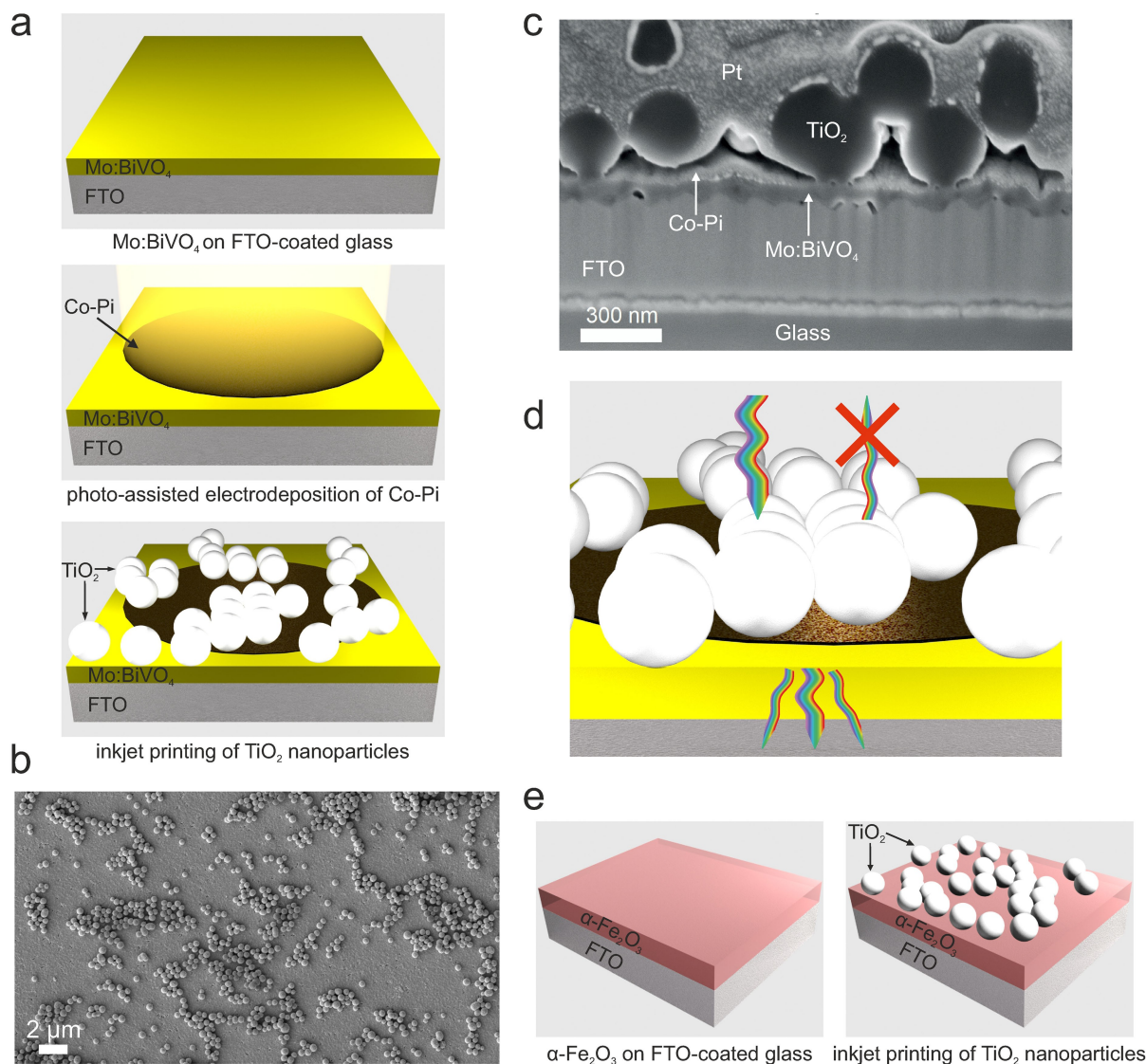
**Figure 1.** (a) Schematic illustration of the fabrication process of Mo:BiVO$_4$/Co–Pi/TiO$_2$ photoanode. (b) Top view SEM image of a fabricated Mo:BiVO$_4$/Co–Pi/TiO$_2$ photoanode (c) SEM cross-sectional image after gold sputtering (10 nm), platinum deposition (protection layer), and focused ion beam milling (FIB). (d) Schematic illustration showing the benefit of the TiO$_2$ nanoparticles for reducing reflection losses and directing the light toward the semiconductor layer. (e) Schematic illustration of the fabrication process of $\alpha$-Fe$_2$O$_3$/TiO$_2$ photoanodes.
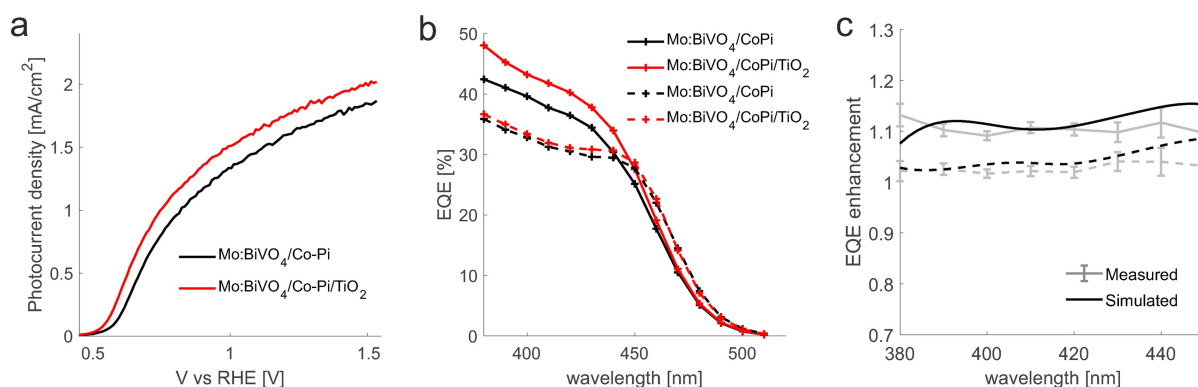


**Figure 2.** (a) Photocurrent density-voltage curves measured in KPi under front illumination. (b) EQE at 1.23 V vs RHE under front (solid curves) and back (dashed curves) illumination. (c) Measured and simulated EQE enhancement spectra under front (solid curves) and back (dashed curves) illumination.

**ChemPhotoChem**

Research Articles
doi.org/10.1002/cptc.202100248

**Chemistry
Europe**
European Chemical
Societies Publishing

simultaneously fitted to the measured EQEs for the bare Mo:BiVO$_4$/Co—Pi samples under front and back illumination to determine the hole diffusion length $L$, the donor density $N_D$ and the charge transfer parameter $R_S$. Finally the EQE spectra under front and back illumination for Mo:BiVO$_4$/Co—Pi/TiO$_2$ including the optical contribution of the nanoparticles were calculated (full procedure described in section "Experimental section & Computational methods"). The simulated EQE spectra are shown in Figure S2. The discrepancy between measured and simulated curves can originate from incomplete charge transport and interfacial transfer modeling in Mo:BiVO$_4$ as well inaccurate Co—Pi optical modeling. Figure 2c shows the EQE enhancement spectra calculated from simulated and measured EQEs. A very good agreement can be observed and the model shows in particular that increased performances are obtained only under front illumination. This suggests that the TiO$_2$ nanoparticles are contributing via an optical effect.

In addition, we used the model to study the influence of the surface coverage on the EQE enhancement obtained, and to check if a similar effect can be obtained with other materials than TiO$_2$ (Figure S4). A surface coverage of 40% was found to

be optimal with respect to lower values. Moreover, a similar optical contribution can be obtained when 300 nm zirconia (ZrO$_2$) nanoparticles are used instead of TiO$_2$. This confirms the applicability of our strategy to other high index dielectric nanoparticles.

## Analysis of the enhancement mechanism

We investigated the origin of the observed enhancement and the reason that it occurs only under front illumination. Figure 3a shows the measured reflectance spectrum in water of Mo:BiVO$_4$/Co—Pi and Mo:BiVO$_4$/Co—Pi/TiO$_2$ samples (measurement procedure described in section "Experimental section & Computational methods"). A pronounced decrease of about 10% in the reflected amount of light happens in the presence of TiO$_2$ nanoparticles (from ~20% to ~10%), showing that the reflection losses are reduced as a result of the interaction between light and the nanoparticles. This decrease is almost constant through the whole spectral range measured. Interestingly, this is quantitatively similar to the enhancement of
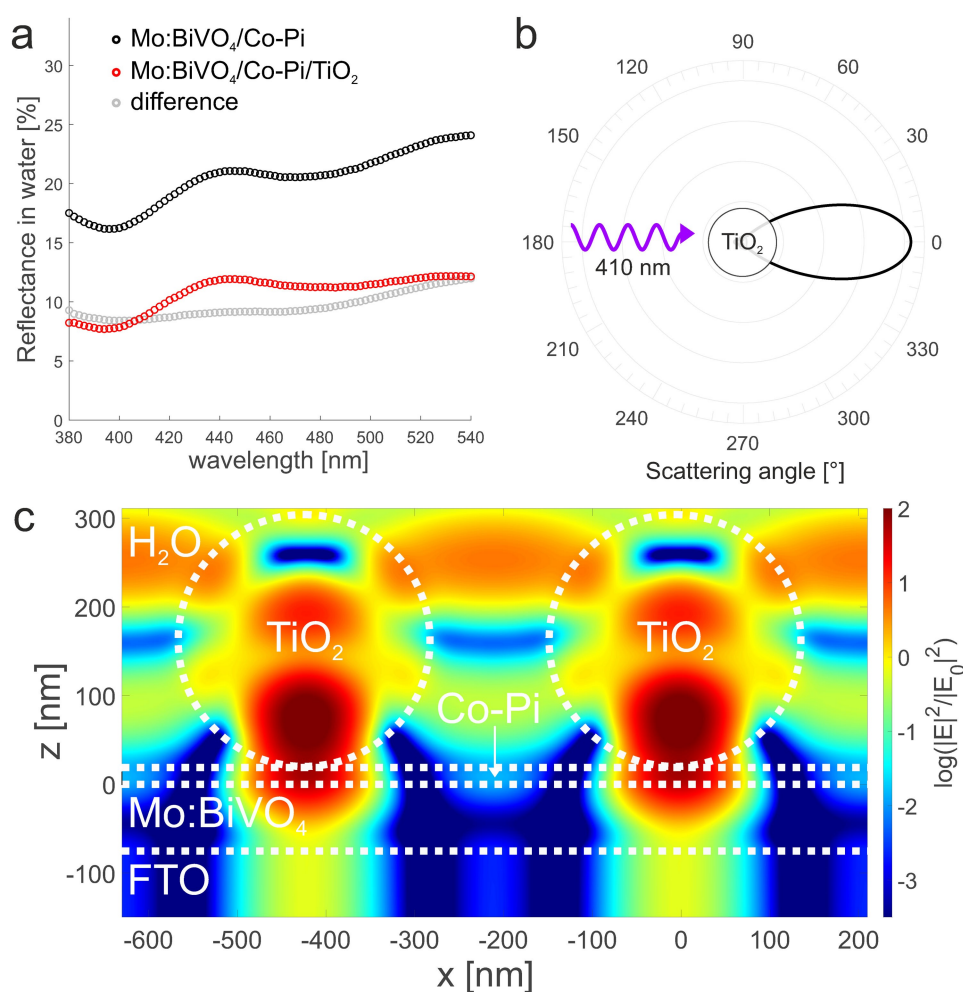


**Figure 3.** (a) Measured reflectance spectra in water for Mo:BiVO$_4$/Co—Pi and Mo:BiVO$_4$/Co—Pi/TiO$_2$ samples. (b) Differential scattering cross section at 410 nm with respect to the scattering angle for an isolated 300 nm TiO$_2$ nanoparticle in water. (c) Electric field intensity map at 410 nm simulated for a Mo:BiVO$_4$/Co—Pi/TiO$_2$ geometry with periodic boundary conditions. Light is incident from the top and the electric field is.polarized in the plane of the cross section.

**ChemPhotoChem**

Research Articles
doi.org/10.1002/cptc.202100248

**Chemistry Europe**
European Chemical
Societies Publishing

photocurrent density and EQE observed under front illumination (Figure 2c).

In order to understand if this interaction can increase the amount of light absorbed in the Mo:BiVO$_4$ layer, we studied the properties of a single 300 nm TiO$_2$ nanoparticle in water with Mie scattering theory.[53] Figure 3b shows the differential scattering cross-section with respect to the scattering angle, upon illumination at 410 nm wavelength corresponding to the high absorption region of Mo:BiVO$_4$. It can be seen that the light scattered by the nanoparticle is almost totally directed forward, showing that the reduced reflectance can result in more light reaching the Mo:BiVO$_4$ layer. The light distribution in a Mo:BiVO$_4$/TiO$_2$ sample was simulated with rigorous coupled wave analysis[54] (RCWA) by assuming a periodic nanoparticles distribution and 40% TiO$_2$ surface coverage. The electric field intensity map at 410 nm is shown in Figure 3c. Hot-spots of the electric field are visible in the Mo:BiVO$_4$ layer exactly below the nanoparticles, as a result of the predominant forward scattering. As a consequence, the overall electric field intensity in Mo:BiVO$_4$ is higher compared to the bare structure (Figure S5).

Increased performances after TiO$_2$ nanoparticles deposition were observed only for photoanodes including Co–Pi catalyst, even though simulations show a similar effect without Co–Pi As most photogenerated charges are located exactly below the nanoparticles (Figure 3c), the poor conductivity of TiO$_2$ could result in reduced charge transfer. The presence of a Co–Pi spacer would then enable the photogenerated charges to be transported to the regions not in contact with nanoparticles. The wetting conditions at the interface with or without Co–Pi could also be impacting the overall performance. This last hypothesis was studied by performing contact angle measurements on Mo:BiVO$_4$ and Mo:BiVO$_4$/Co–Pi (Figure S6). The case of $\alpha$-Fe$_2$O$_3$ was also studied (section "TiO$_2$ nanoparticles deposited on $\alpha$-Fe$_2$O$_3$ photoanodes"). The surface of Mo:BiVO$_4$/Co–Pi and $\alpha$-Fe$_2$O$_3$ is considerably more hydrophilic than Mo:BiVO$_4$. Therefore, we suggest that when Mo:BiVO$_4$ is decorated with TiO$_2$ nanoparticles, water does not fully penetrate inside the tiny spaces be tween the nanoparticles and the underneath layers (Figure S6d). These regions have a high contribution to the photocurrent (Figure 3c), which explains why enhanced performances are not observed. Further investigation of the non-optical contributions of TiO$_2$ nanoparticles could be made with characterization techniques such as electrochemical impedance spectroscopy, and is beyond the scope of the present work which focuses on analyzing the optical contributions.

The stability of Mo:BiVO$_4$/Co–Pi and Mo:BiVO$_4$/Co–Pi/TiO$_2$ electrodes was also studied (Figure S7), showing that the photocurrent density of Mo:BiVO$_4$/Co–Pi/TiO$_2$ decreases faster than Mo:BiVO$_4$/Co–Pi. As a consequence, both samples show a similar photocurrent density after 10 min. The decreasing performances with time for both sample matches the conclusion of previous reports about the modest stability of Co–Pi in neutral conditions.[39,45,48] The faster degradation for Mo: BiVO$_4$/Co–Pi/TiO$_2$ can be explained by the very different light intensity profile compared to Mo:BiVO$_4$/Co–Pi. It can be seen on Figu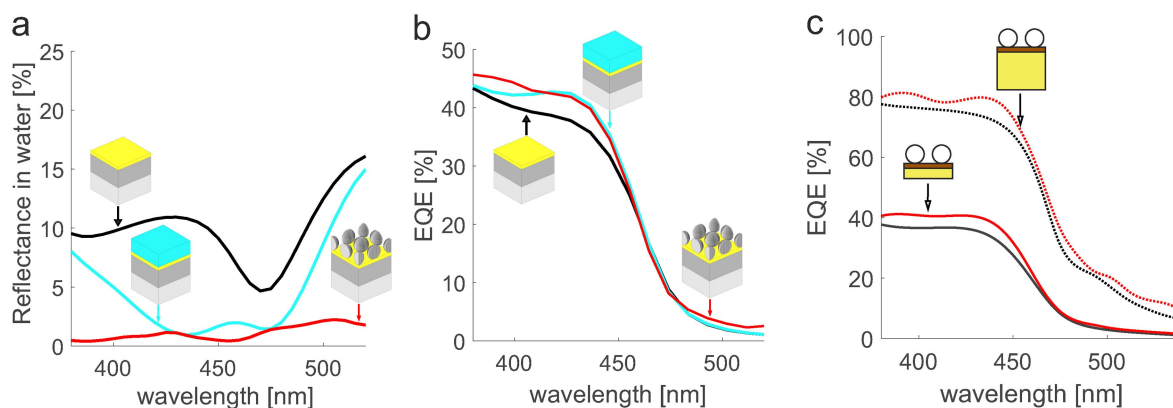re 3c that the light intensity is very high in the regions located below the nanoparticles, which are contributing the most to the photocurrent. For Mo:BiVO$_4$/Co–Pi, the light absorption is ruled by the Beer-Lambert law (Figure S5). This hypothesis was confirmed by studying the stability of Mo: BiVO$_4$/Co–Pi under concentrated illumination (10 suns, Figure S8). A faster degradation is observed compared to non-concentrated illumination.

We analyzed the optical contribution of the TiO$_2$ nanoparticles with respect to AR layers. Covering BiVO$_4$ with such layers cannot be used as a beneficial strategy for water-splitting if there is no proper energy band alignment enabling efficient extraction of the photogenerated charges. Our method for modeling optical enhancement in water splitting photoelectrodes[32] assumes that the semiconductor/electrolyte charge transfer parameter is equal for both the bare sample and the sample including an optical enhancement strategy, which is a wrong assumption in this case.However, the model can be used to study the optical contribution. We simulated, therefore, a geometry including a 300 nm layer of refractive index $n = 1.8$ on top of BiVO$_4$, which yields almost no reflectance in water in the range 430–470 nm, similar to BiVO$_4$/TiO$_2$ (Figure 4a). The simulated EQE is shown in Figure 4b. It can be seen that the EQE of the sample with the AR layer is very similar to BiVO$_4$/TiO$_2$ in the interval 430–470 nm, but the effect decreases at lower and higher wavelengths. It can be concluded that the optical contribution of TiO$_2$ nanoparticles is quantitatively equivalent to a set of AR layers optimized for the whole spectrum.

Finally, we studied the applicability of the presented strategy to a thick BiVO$_4$ electrode with optimal charge transport properties. A BiVO$_4$/Co–Pi geometry with 380 nm BiVO$_4$ film thickness was considered (about 5 times thicker than our fabricated sample). The EQE of BiVO$_4$/Co–Pi and BiVO$_4$/Co–Pi/TiO$_2$ were calculated by assuming an optimal hole diffusion length of 300 nm. The other parameters were kept the same as our fabricated sample. Similar diffusion lengths have been experimentally reported in BiVO$_4$ electrodes where shallow doping is achieved with a post-treatment.[12] A similar optical enhancement to our fabricated sample is found in EQE (Figure 4c), corresponding to 10% increase in photocurrent density under AM1.5G illumination (from 3.28 mA/cm$^2$ to 3.60 mA/cm$^2$). The reflected amount of light being similar for the 75 nm and 380 nm samples, this result suggests that this strategy can improve photoanodes suffering from high reflection losses regardless of the bare sample performance.

## TiO$_2$ nanoparticles deposited on α-Fe$_2$O$_3$ photoanodes

In order to study the applicability of this strategy to other semiconductor materials, the effect of depositing high refractive index TiO$_2$ nanoparticles on a hematite photoanode was investigated. Similarly to BiVO$_4$, $\alpha$-Fe$_2$O$_3$ has a high refractive index which induces considerable reflection losses at the electrolyte/semiconductor interface under front illumination ($n = 3.3/3.0$ at 450 nm for $\alpha$-Fe$_2$O$_3$/ BiVO$_4$[55,56]). Amorphous TiO$_2$ nanoparticles with an average diameter of 300 nm were

**ChemPhotoChem**

Research Articles
doi.org/10.1002/cptc.202100248

**Chemistry Europe**
European Chemical
Societies Publishing

**Figure 4.** (a) Simulated reflectance spectra in water for $BiVO_4$ and $BiVO_4/TiO_2$, and a geometry including a 300 nm layer of refractive index 1.8 on top of $BiVO_4$. (b) Simulated EQE spectra under front illumination by assuming an equal semiconductor/electrolyte charge transfer parameter for the different configurations. (c) Simulated EQEs under front illumination for $BiVO_4/Co$–$Pi$ and $BiVO_4/Co$–$Pi/TiO_2$ corresponding to the fabricated electrode (solid curves, 75 nm $BiVO_4$, $L = 62$ nm) and a thicker electrode with optimal hole diffusion length (dotted curves, 380 nm $BiVO_4$, $L = 300$ nm).

deposited with inkjet printing on the surface of a 95 nm $\alpha$-$Fe_2O_3$ film fabricated with electrodeposition from an iron precursor and a two-steps annealing procedure (detailed fabrication procedure in the section "Experimental section & Computational methods"). The inkjet printing process is repeated until a surface coverage of about 40% is reached (Figure 5a).

The photocurrent density before and after $TiO_2$ nanoparticles deposition was measured in 1 M NaOH (pH = 14).

Figure 5b shows that an increased photocurrent density by about 10% at high applied voltage is observed under front illumination upon nanoparticles deposition. Under back illumination, the performances of $\alpha$-$Fe_2O_3$ and $\alpha$-$Fe_2O_3/TiO_2$ are similar (Figure S9). The influence of the surface coverage on the photoelectrochemical performances was studied by varying the quantity of $TiO_2$ nanoparticles deposited (Figure 5c). The values were estimated from optical microscope images. The result shows that the enhancement increases with the surface cover-
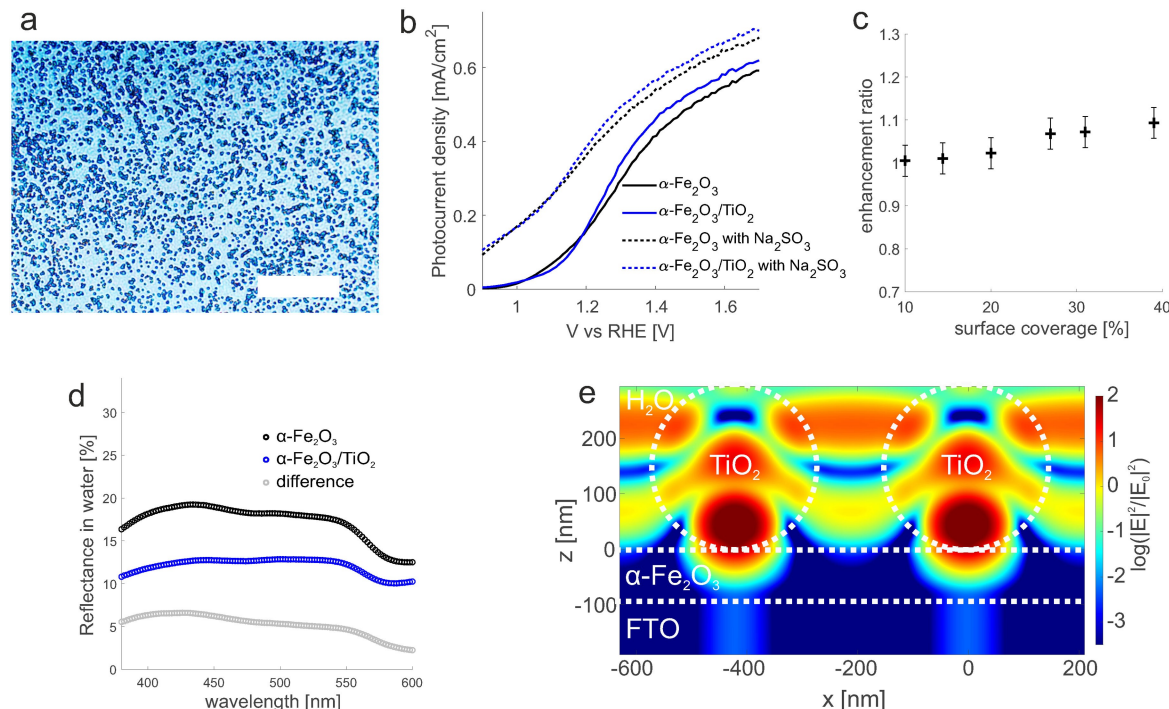


**Figure 5.** (a) Optical microscope image (in reflection mode) showing $TiO_2$ nanoparticles deposited on a $\alpha$-$Fe_2O_3$ film. The scale bar is 25 $\mu$m. (b) Photocurrent density–voltage curves measured under front illumination for 40% $TiO_2$ surface coverage. (c) Photocurrent enhancement ratio (averaged between 1.3 and 1.6 V vs RHE) under front illumination in 1 M NaOH. (d) Measured reflectance spectra in water for $\alpha$-$Fe_2O_3$ and $\alpha$-$Fe_2O_3/TiO_2$ samples. (e) Electric field intensity map at 410 nm simulated for a $Mo:BiVO_4/Co$–$Pi/TiO_2$ with periodic boundary conditions. Light is incident from the top and the electric field is polarized in the plane of the cross section.

**ChemPhotoChem**

Research Articles
doi.org/10.1002/cptc.202100248

**Chemistry
Europe**
European Chemical
Societies Publishing

age. The photocurrent density reaches 0.53 mA/cm² at 1.5 V vs RHE for the $\alpha$-Fe$_2$O$_3$/TiO$_2$ sample with about 40% surface coverage. Further insights on the physical phenomena explaining the enhanced performances were gained by measuring the photocurrent density-voltage in a solution containing additionally 0.5 M Na$_2$SO$_3$ as a hole scavenger (Figure 5b), such that 100% hole injection efficiency can be assumed for $\alpha$-Fe$_2$O$_3$ and $\alpha$-Fe$_2$O$_3$/TiO$_2$. The enhancement is smaller compared to the previous case (enhancement of 1.09 and 1.04, averaged between 1.3-1.6 V vs RHE, without and with hole scavenger, respectively), which indicates that the addition of nanoparticles is also decreasing the amount of surface recombinations.

The reflectance in water (Figure 5d) is decreased upon deposition of TiO$_2$ nanoparticles However, the effect is weaker compared to Mo:BiVO$_4$/Co–Pi (~5% decrease compared to ~10% in Figure 5a). The decrease in reflectance matches quantitatively the photocurrent enhancement in hole scavenger electrolyte under front illumination. This suggests that the anti-reflective effect of the TiO$_2$ nanoparticles is the origin for the observed enhancement. Moreover, the simulated electric field intensity distribution in a $\alpha$-Fe$_2$O$_3$/TiO$_2$ geometry (Figure 5e) shows a similar effect compared to Mo:BiVO$_4$/Co–Pi. As a result of the interaction of light with the nanoparticles, hot spots are visible in $\alpha$-Fe$_2$O$_3$ exactly below the nanoparticles. We studied the stability of $\alpha$-Fe$_2$O$_3$ and $\alpha$-Fe$_2$O$_3$/TiO$_2$ in electrolyte with and without sacrificial hole scavenger (Figure S10). Contrary to Mo:BiVO$_4$/Co–Pi, no faster performance degradation was observed with TiO$_2$ decoration.

## Comparison with plasmonic nanoparticles

We finally compared the effect of TiO$_2$ nanoparticles with respect to enhancement strategies using plasmonic nanoparticles. Mie scattering theory was applied to TiO$_2$ nanoparticles as well as

70 nm Ag@SiO$_2$ nanoparticles that were reported to enhance optically the PEC performances of BiVO$_4$ under back illumination thanks to their plasmonic properties.[25,32] Figure 6a shows the differential scattering efficiency with respect to the scattering angle at 410 nm for a 300 nm TiO$_2$ nanoparticle, a 70 nm Ag@SiO$_2$ nanoparticle (10 nm shell thickness) and a TiO$_2$ nanoparticle of the same size. We define the differential scattering efficiency as the average of the scattering matrix elements[53] for parallel and perpendicular polarization, normalized such that the integral over $4\pi$ steradians is equal to the overall scattering efficiency: [Eq. (1)]

$$q_{eff}(\theta) = \frac{|S_{11}(\theta)|^2 + |S_{22}(\theta)|^2}{2} \cdot \frac{1}{K} \qquad (1)$$

where $K$ is chosen such that $\int q_{eff}\, d\Omega = Q_{scat}$. The scattering efficiency $Q_{scat}$ for the three types of nanoparticles is shown in Figure 6b and defined as: [Eq. (2)]

$$Q_{scat}(\lambda) = \frac{C_{scat}(\lambda)}{\pi r^2} \qquad (2)$$

where $C_{scat}(\lambda)$ is the scattering cross section and $\pi r^2$ is the physical cross section of the nanoparticle. The corresponding absorption efficiency spectra are shown in Figure S11. It can be seen that even if the overall scattering efficiency is almost equivalent between 300 nm TiO$_2$ and Ag@SiO$_2$ nanoparticles at 410 nm, the amount of forward scattering is much higher for TiO$_2$. Conversely, Ag@SiO$_2$ nanoparticles provide a higher amount of back-scattering and give rise to absorption losses. This can explain why clear evidence of optically enhanced performances as a result of plasmonic effects were mostly obtained under back illumination[25,31] whereas our strategy is effective only under front illumination. The scattering efficiency spectrum of the 300 nm TiO$_2$ nanoparticle shows two resonant
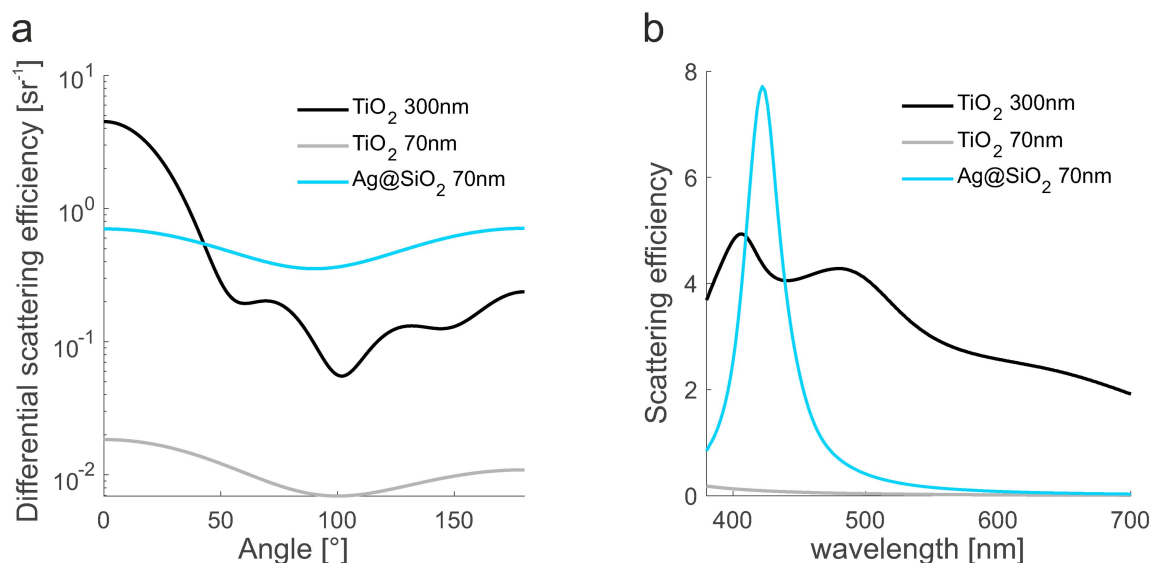


**Figure 6.** (a) Differential scattering efficiency with respect to the scattering angle at 410 nm for isolated nanoparticles in water. The direction of the incident light corresponds to 180°. (b) Scattering efficiency spectra.

**ChemPhotoChem**

Research Articles
doi.org/10.1002/cptc.202100248

**Chemistry Europe**
European Chemical
Societies Publishing

features are present at 410 nm and 500 nm which are identified as high order multipoles (Figure S12).

## Conclusion

In conclusion, depositing large $TiO_2$ nanoparticles at the surface of $Mo:BiVO_4/Co-Pi$ and $\alpha$-$Fe_2O_3$ resulted in optically increased photoelectrochemical performances under front illumination by about 10% for $Mo:BiVO_4/Co-Pi$ and 5% for $\alpha$-$Fe_2O_3$. We showed that the effect originates from almost 100% of the incident light being scattered forward by the nanoparticles, reducing reflection losses and increasing the amount of light absorbed close the semiconductor/electrolyte interface in the active material layer. The observed enhancement values were validated quantitatively under front and back illumination with a theoretical method studying the contribution of optical effects in water-splitting photoelectrodes. We found that the optical effect of the $TiO_2$ nanoparticles is quantitatively similar to AR coatings optimized for the whole spectrum. The applicability of this strategy to an optimized was theoretically studied, and the results suggested that the enhancement does not depend on the amount of bulk and surface recombination in the bare sample. .Finally, an analysis was performed to understand the benefit with respect to strategies using plasmonic nanoparticles. Our approach has the advantage of using inexpensive, non absorbent, highly chemically resistant nanoparticles having high refractive indices such as $TiO_2$ or $ZrO_2$ instead of noble metals. It is an easy procedure to implement, and we demonstrated that it is compatible with large-scale production techniques such as inkjet printing. Other deposition techniques such as blade coating or spin-coating could be used as well. Our method can be used to address the problem of high reflection losses at the semiconductor/electrolyte interface under front illumination and, as a consequence, can be applied in parallel to other techniques for improving metal oxide photoanodes, such as post-treatment doping, OER catalysts and optical strategies such as nanostructuring and back-reflecting layers. This could be highly beneficial for improving the solar-to-hydrogen efficiency of existing PEC water-splitting devices including a front-illuminated $BiVO_4$[8,35-41] or $\alpha$-$Fe_2O_3$[40,42-44] photoanode. We therefore believe that this effect can help bringing the performance of water-splitting materials closer to their theoretical limit.

## Experimental section & Computational methods

### $Mo:BiVO_4$ film fabrication

$Mo:BiVO_4$ films were fabricated using a sol-gel method adapted from Ref. [7]. A solution containing 50 mM bismuth, 46.5 mM vanadium and 3.5 mM molybdenum was prepared with the following procedure. 121.3 mg of $Bi(NO_3)_3.5H_2O$ (Sigma-Aldrich) was dissolved in 4 ml of 20:1 acetic acid/acetylacetone. Then, 61.7 mg of $V(O)(acac)_2$ (Sigma-Aldrich) was added and dissolved by stirring the solution in a 60 °C water bath for 5 min. A rapid optimization involving drop-casting of the solution on FTO, subsequent annealing at 550 °C and

photocurrent density measurement under front illumination in aqueous electrolyte was performed to select the molybdenum doping value (Figure S13). It was found that 7% Mo and a V/Bi ratio of 0.93 produces the highest photocurrent density.

A second solution containing 35 mM molybdenum was prepared in parallel by dissolving 31.0 mg $(NH_4)_6Mo_7O_2 4.4H_2O$ (Sigma-Aldrich) in 0.5 ml deionized water, followed by addition acetic acid/acetylacetone (20:1) such that the total volume is 5 ml. Finally, 0.5 ml of the molybdate solution was added to the solution containing Bi and V precursors and 20:1 acetic acid/acetylacetone was added such that the total volume is 5 ml.

FTO-coated glass substrates (TCO22-15, Solaronix) were cleaned at 60 °C in an ultrasonic bath containing 2% cleaning solution (Micro-90) for 15 min, followed by 45 min drying in air at 100 °C. An oxygen plasma cleaning (Diener Nano) was finally performed for 10 min immediately before the next step. Several deposition cycles were performed to reach the final $Mo:BiVO_4$ thickness. Each cycle consisted in spin-coating the solution (2000 rpm, 40 s) followed by 10 min annealing in air at 450 °C. The influence of the number of deposition cycles on the final PEC performances is shown in Figure S14. Similar performances are observed from 4 to 8 cycles under front illumination. Therefore a value of 5 cycles was selected, corresponding to ~75 nm $Mo:BiVO_4$ thickness. When the final number of deposition cycles was reached, a final annealing in air for 2 h at 550 °C was performed (2 °C/min increase, cooling down to room temperature). The deposition of $Mo:BiVO_4$ was made using 5 cm×5 cm FTO plates as substrate. At the end of the $Mo:BiVO_4$ fabrication process, each 5 cm×5 cm plate was cut into four 2.5 cm×2.5 cm samples for subsequent deposition of Co-Pi and TiO2 nanoparticles.

### Co-Pi deposition

Photoassisted electrodeposition of a Co-Pi OER catalyst was performed by using the procedure reported in Ref. [15]. A solution of 0.15 mM $Co(NO_3)_2·6H_2O$ (Alfa Aesar) in 0.1 M $K_2HPO_4/KH_2PO_4$ potassium phosphate buffer at pH = 7 was prepared. Co-Pi deposition on $Mo:BiVO_4$ was then performed under AM1.5G illumination with a bias of 0.3 V vs Ag/AgCl. The optimal deposition time was found to be 400 s (Figure S15). The resulting Co-Pi films were finally rinsed with deionized water and dried under a flow of nitrogen.

### $\alpha$-$Fe_2O_3$ film fabrication

$\alpha$-$Fe_2O_3$ photoanodes were fabricated by using the electrodeposition procedure described in Ref. [57] on 2.5 cm×2.5 cm FTO substrates. The optimal deposition time was found to be 40 s. A two step annealing process was performed after the deposition step. The samples were first annealed for 4 h at 550 °C (5 °C/min increase, cooling down to room temperature). Then, a short 15 min annealing at 800 °C was performed. The increased performances obtained upon this second annealing step were attributed to tin doping of $\alpha$-$Fe_2O_3$ arising from thermal diffusion of Sn(IV) from the FTO substrate. The final thickness of the $\alpha$-$Fe_2O_3$ films is about 95 nm.

### $TiO_2$ nanoparticles deposition

Amorphous titania nanoparticles with an average size of 300 nm (Creative Diagnosis) were printed on the surface of the photoelectrodes with a multi-nozzle inkjet printer (Ceradrop F-serie). The solvent was selected as a mixture of 75% deionized water and 25% ethanol. Homogeneous surface coverage of the samples was achieved by dispensing 10 pL droplets in a square pattern. For

**ChemPhotoChem**

Research Articles
doi.org/10.1002/cptc.202100248

**Chemistry**
**Europe**
European Chemical
Societies Publishing

deposition on Mo:BiVO$_4$/Co—Pi, the splat diameter was set to 50 $\mu$m based on scanning electron microscope (SEM) images. The inkjet printing process was repeated several times to reach the desired nanoparticles surface coverage (~40% coverage, Figure 1b). The homogeneity of the nanoparticles deposition (reduced "coffee-ring" effect) was found to be improved when the samples were immersed in 1 M aqueous NaOH for 45 s immediately before the printing step. We verified that this pre-treatment does not modify the PEC performances of the samples. For $\alpha$-Fe$_2$O$_3$ samples, an 30 s oxygen plasma cleaning step was performed immediately before nano-particles deposition, and the splat diameter was set to 100 $\mu$m.

**Photoelectrochemical characterization**

Photocurrent density under applied bias and external quantum efficiency (EQE) measurements were performed in a photoelectrochemical cell (PECC-2, Zahner Elektrik) using a Ag/AgCl reference electrode and a Pt wire as counter electrode. A mask was used to limit the illuminated area to 0.64 cm$^2$. The photocurrent density was measured under simulated AM1.5G illumination (ScienceTec solar simulator). The light intensity was calibrated before each measurement to 100 mW/cm$^2$ at the measurement plane with a silicon photodiode. EQE measurements were performed using a halogen lamp as the light source and a monochromator with ~10 nm band-pass (Newport). All the necessary wavelengths for constructing the EQE spectrum were consecutively switched on in a single chronoamperometric measurement at 1.23 V vs RHE. This was first done with the PEC cell where the sample is the working electrode and then with a calibrated photodiode. The EQE spectra were finally extracted with a Matlab post- processing as [Eq. (3)]:

$$EQE(\lambda) = \frac{hc}{e} \frac{j_{ph}}{\lambda P_0(\lambda)} \quad (3)$$

where $j_{ph}(\lambda)$ is the photocurrent density under quasi-monochromatic illumination, $P_0$ is the incident power and $hc/e \approx 1240$ eV.nm. Performance comparison between Mo:BiVO$_4$/Co- Pi and Mo:BiVO$_4$/Co—Pi/TiO$_2$ was made between samples diced from the same original 5 cm × 5 cm plate with Mo:BiVO$_4$. The good reproducibility of the Co—Pi deposition and TiO$_2$ printing as well as the small experimental uncertainty in J—V curve/EQE measurements was confirmed by measuring two Mo:BiVO$_4$/Co—Pi/TiO$_2$ samples supposedly identical (Figure S16). This result was used to extract the error bars that appear in EQE curves in the following. The performances of $\alpha$-Fe$_2$O$_3$ and $\alpha$-Fe$_2$O$_3$/TiO$_2$ were compared by measuring the photocurrent density before and after nanoparticles deposition.

**Theoretical analysis**

Electromagnetic simulations were performed with RCWA under periodic boundary conditions. The simulated geometries were designed to realistically match our SEM/optical microscope characterization of fabricated Mo:BiVO$_4$/Co—Pi/TiO$_2$ and $\alpha$-Fe$_2$O$_3$/TiO$_2$ samples. Figure S17 show sketches of the Mo:BiVO$_4$/Co—Pi and Mo:BiVO$_4$/Co—Pi/TiO$_2$ geometries that were simulated. The Mo:BiVO$_4$ thickness was set to 75 nm, the $\alpha$-Fe$_2$O$_3$ thickness was set to 95 nm and the nanoparticles diameter was set to 300 nm. The Co—Pi thickness was set to 20 nm. The refractive index of FTO, Mo:BiVO$_4$, $\alpha$-Fe$_2$O$_3$ and TiO$_2$ were taken from Refs. [47,56,55,58]. A spectrally constant value of $3.2 + 0.05i$ was used for the refractive index of Co—Pi. To compare the designed geometry with respect to the real samples and validate the optical constants used to describe the materials, the measured absorbance and reflectance of Mo:BiVO$_4$/Co—Pi and $\alpha$-Fe$_2$O$_3$ was compared with simulations. A good agreement was found in both cases (Figures S18 and S19). Analysis

of the measured EQE with the method for modeling optical enhancement in water splitting photoelectrodes was performed for Mo:BiVO$_4$/Co—Pi and Mo:BiVO$_4$/Co—Pi/TiO$_2$ according to the procedure described in Ref. [32]. The main assumptions of the charge transport model are: (i) no majority carrier transport limitations (ii) negligible recombination at the Mo:BiVO$_4$/FTO interface. Comparison between front and back photocurrent densities and EQEs for different Mo:BiVO$_4$ film thickness (Figure S14) shows that PEC performances are always higher under front illumination. In addition, the back illumination performances decrease when the film thickness is increased, whereas the front illumination photocurrent density is almost constant. This indicates that electron transport is not a limitation in contrast to hole transport. In order to reduce back-contact recombination, the beneficial effect of a thin hole-blocking SnO$_2$ layer between FTO and Mo:BiVO$_4$ was investigated in agreement with previous reports.[10,59] No increase in photocurrent density was found compared to the sample without SnO$_2$ (Figure S20), and the performances were reduced when the SnO$_2$ thickness was increased. It can therefore be concluded that recombination at the Mo:BiVO$_4$/FTO interface are negligible even without a hole-blocking layer. This validates the applicability of the model.

The calculated EQEs under front and back illumination was first fitted to the experimentally measured spectra for Mo:BiVO$_4$/Co—Pi to determine the hole diffusion length $L$, the donor density $N_D$ and the hole transfer efficiency $R_s$.[32] The optimized values are 62.3 nm, $3.97 \times 10^{20}$ cm$^{-3}$ and 0.91, respectively, and the coefficient of determination is $R^2 = 0.95$. The value of $L$ is in line with the previous reports on BiVO$_4$,[60] and the higher donor density compared to pure BiVO$_4$[61] is originating from the molybdenum doping. These values of $L$, $N_D$ and $R_s$ were used to calculate the EQE of the Mo:BiVO$_4$/Co—Pi/TiO$_2$ sample.

**Optical measurements**

Optical measurements of the reflectance and transmittance spectrum are performed with a UV/Visible/Near-Infrared spectrometer (Perkin-Elmer Lambda 1050) without an integrating sphere. For performing measurements with light incident from water (Figures 3a and 5d), a drop of deionized water was dispensed on the sample and a thin glass plate was placed on top of it.

## Conflict of Interest

The authors declare no conflict of interest.

## Data Availability Statement

The data that support the findings of this study are available from the corresponding author upon reasonable request.

[1] J. Nowotny, T. Bak, D. Chu, S. Fiechter, G. E. Murch, T. N. Veziroglu, *Int. J. Hydrogen Energy* **2014**, *39*, 4151–4157.

[2] K. Sivula, R. van de Krol, *Nat. Rev. Mater.* **2016**, 15010.

[3] M. Gratzel, *Nature* **2001**, *414*, 338–344.

[4] R. Van De Krol, M. Gr"atzel, *Photoelectrochemical Hydrogen Production*, Springer US, 2012.

[5] T. W. Kim, K.-S. Choi, *Science* **2014**, *343*, 990–994.

[6] K. J. McDonald, K.-S. Choi, *Energy Environ. Sci.* **2012**, *5*, 8553–8557.

[7] P. M. Rao, L. Cai, C. Liu, I. S. Cho, C. H. Lee, J. M. Weisse, P. Yang, X. Zheng, *Nano Lett.* **2014**, *14*, 1099–1105.

[8] Y. Pihosh, I. Turkevych, K. Mawatari, J. Uemura, Y. Kazoe, S. Kosar, K. Makita, T. Sugaya, T. Matsui, D. Fujita, M. Tosa, M. Kondo, T. Kitamori, *Sci. Rep.* **2015**, *5*, 11141.

[9] J. A. Seabold, K. Zhu, N. R. Neale, *Phys. Chem. Chem. Phys.* **2014**, *16*, 1121–131.

[10] Y. Liang, T. Tsubota, L. P. Mooij, R. Van De Krol, *J. Phys. Chem. C* **2011**, *115*, 17594–17598.

[11] W.-J. Yin, S.-H. Wei, M. M. Al-Jassim, J. Turner, Y. Yan, *Phys. Rev. B* **2011**, *83*, 155102.

[12] J.-W. Jang, D. Friedrich, S. Mu"ller, M. Lamers, H. Hempel, S. Lardhi, Z. Cao, M. Harb, L. Cavallo, R. Heller, R. Eichberger, R. van de Krol, F. F. Abdi, *Adv. Energy Mater.* **2017**, *7*, 1701536.

[13] G. Wang, Y. Ling, X. Lu, F. Qian, Y. Tong, J. Z. Zhang, V. Lordi, C. Rocha Leao, Y. Li, *J. Phys. Chem. C* **2013**, *117*, 10957–10964.

[14] J. K. Cooper, S. B. Scott, Y. Ling, J. Yang, S. Hao, Y. Li, F. M. Toma, M. Stutzmann, K. V. Lakshmi, I. D. Sharp, *Chem. Mater.* **2016**, *28*, 5761–5771.

[15] S. K. Pilli, T. E. Furtak, L. D. Brown, T. G. Deutsch, J. A. Turner, A. M. Herring, *Energy Environ. Sci.* **2011**, *4*, 5028–5034.

[16] D. K. Zhong, M. Cornuz, K. Sivula, M. Gr"atzel, D. R. Gamelin, *Energy Environ. Sci.* **2011**, *4*, 1759–1764.

[17] Z. Chen, H. N. Dinh, E. Miller, *Photoelectrochemical water splitting*, Springer, New York, 2013.

[18] F. Boudoire, R. Toth, J. Heier, A. Braun, E. C. Constable, *Energy Environ. Sci.* **2014**, *7*, 2680–2688.

[19] J. K. Kim, X. Shi, M. J. Jeong, J. Park, H. S. Han, S. H. Kim, Y. Guo, T. F. Heinz, S. Fan, C.-L. Lee, J. H. Park, X. Zheng, *Adv. Energy Mater.* **2018**, *8*, 1701765.

[20] L. Zhang, L. O. Herrmann, J. J. Baumberg, *Sci. Rep.* **2015**, *5*, 16660.

[21] P. S. Archana, N. Pachauri, Z. Shan, S. Pan, A. Gupta, *J. Phys. Chem. C* **2015**, *119*, 15506–15516.

[22] S. A. Maier, *Plasmonics : fundamentals and applications*, Springer, New York, 2007.

[23] L. Mascaretti, A. Dutta, Š. Kment, V. M. Shalaev, A. Boltasseva, R. Zbo˘ril, A. Naldoni, *Adv. Mater.* **2019**, *31*, 1805513.

[24] E. Thimsen, F. Le Formal, M. Gr"atzel, S. C. Warren, *Nano Lett.* **2011**, *11*, 35–43.

[25] F. F. Abdi, A. Dabirian, B. Dam, R. Van De Krol, *Phys. Chem. Chem. Phys.* **2014**, *16*, 15272–15277.

[26] P. Peerakiatkhajohn, J. H. Yun, H. Chen, M. Lyu, T. Butburee, L. Wang, *Adv. Mater.* **2016**, 6405–6410.

[27] E. R. Encina, E. A. Coronado, *J. Phys. Chem. C* **2018**, *122*, 4589–4599.

[28] J. B. Khurgin, *Nat. Nanotechnol.* **2015**, *10*, 2–6.

[29] H. Dotan, K. Sivula, M. Gr"atzel, A. Rothschild, S. C. Warren, *Energy Environ. Sci.* **2011**, *4*, 958–964.

[30] D. K. Zhong, S. Choi, D. R. Gamelin, *J. Am. Chem. Soc.* **2011**, *133*, 18370–18377.

[31] M. Valenti, D. Dolat, G. Biskos, A. Schmidt-Ott, W. A. Smith, *J. Phys. Chem. C* **2015**, *119*, 2096–2104.

[32] L. Driencourt, B. Gallinet, C. E. Housecroft, S. Fricke, E. C. Constable, *J. Phys. Chem. C* **2021**, *125*, 7010–7021.

[33] K. Sivula, F. Le Formal, M. Gr"atzel, *ChemSusChem* **2011**, *4*, 432–449.

[34] A. G. Tamirat, J. Rick, A. A. Dubale, W.-N. Su, B.-J. Hwang, *Nanoscale Horiz.* **2016**, *1*, 243–267.

[35] Y. Qiu, W. Liu, W. Chen, W. Chen, G. Zhou, P.-C. Hsu, R. Zhang, Z. Liang, S. Fan, Y. Zhang, Y. Cui, *Sci. Adv.* **2016**, *2*, e1501764.

[36] P. Chakthranont, T. R. Hellstern, J. M. McEnaney, T. F. Jaramillo, *Adv. Energy Mater.* **2017**, *7*, 1701515.

[37] X. Shi, K. Zhang, K. Shin, M. Ma, J. Kwon, I. T. Choi, J. K. Kim, H. K. Kim, D. H. Wang, J. H. Park, *Nano Energy* **2015**, *13*, 182–191.

[38] C. Pornrungroj, V. Andrei, M. Rahaman, C. Uswachoke, H. J. Joyce, D. S. Wright, E. Reisner, *Adv. Funct. Mater.* **2020**, *31*, 2008182.

[39] J. H. Kim, Y. Jo, J. H. Kim, J. W. Jang, H. J. Kang, Y. H. Lee, D. S. Kim, Y. Jun, J. S. Lee, *ACS Nano* **2015**, *9*, 11820–11829.

[40] J. H. Kim, J.-W. Jang, Y. H. Jo, F. F. Abdi, Y. H. Lee, R. van de Krol, J. S. Lee, *Nat. Commun.* **2016**, *7*, 13380.

[41] L. Han, F. F. Abdi, R. Van De Krol, R. Liu, Z. Huang, H.-J. Lewerenz, B. Dam, M. Zeman, A. H. M. Smets, *ChemSusChem* **2014**, *7*, 2832–2838.

[42] J.-W. Jang, C. Du, Y. Ye, Y. Lin, X. Yao, J. Thorne, E. Liu, G. McMahon, J. Zhu, A. Javey, J. Guo, D. Wang, *Nat. Commun.* **2015**, *6*, 7447.

[43] J. Brillet, J. H. Yum, M. Cornuz, T. Hisatomi, R. Solarska, J. Augustynski, M. Graetzel, K. Sivula, *Nat. Photonics* **2012**, *6*, 824–828.

[44] J. Park, K.-Y. Yoon, T. Kim, H. Jang, M.-J. Kwak, J. Y. Kim, J.-H. Jang, *Nano Energy* **2020**, *76*, 105089.

[45] P. Bornoz, F. F. Abdi, S. D. Tilley, B. Dam, R. van de Krol, M. Graetzel, K. Sivula, *J. Phys. Chem. C* **2014**, *118*, 16959–16966.

[46] M. A. de Arau'jo, D. Coelho, L. H. Mascaro, E. C. Pereira, *J. Solid State Electrochem.* **2018**, *22*, 1539–1548.

[47] P. Cendula, L. Steier, P. A. Losio, M. Gr"atzel, J. O. Schumacher, *Adv. Funct. Mater.* **2018**, *28*, 1702768.

[48] J. H. Kim, J. S. Lee, *Adv. Mater.* **2019**, *31*, 1806938.

[49] J. Zhao, Y. Guo, L. Cai, H. Li, K. X. Wang, I. S. Cho, C. H. Lee, S. Fan, X. Zheng, *ACS Energy Lett.* **2016**, *1*, 68–75.

[50] S. S. Kalanur, I.-H. Yoo, J. Park, H. Seo, *J. Mater. Chem. A* **2017**, *5*, 1455–1461.

[51] X. Yang, R. Liu, C. Du, P. Dai, Z. Zheng, D. Wang, *ACS Appl. Mater. Interfaces* **2014**, *6*, 12005–12011.

[52] Y. Fu, C. L. Dong, W. Zhou, Y. R. Lu, Y. C. Huang, Y. Liu, P. Guo, L. Zhao, W. C. Chou, S. Shen, *Appl. Catal. B* **2020**, *260*.

[53] C. F. Bohren, D. R. Huffman, *Absorption and scattering of light by small particles*, Wiley, New York, 2008.

[54] M. G. Moharam, E. B. Grann, D. A. Pommet, T. K. Gaylord, *J. Opt. Soc. Am. A* **1995**, *12*, 1068–1076.

[55] G. Segev, H. Dotan, D. S. Ellis, Y. Piekner, D. Klotz, J. W. Beeman, J. K. Cooper, D. A. Grave, I. D. Sharp, A. Rothschild, *Joule* **2018**, *2*, 210–224.

[56] J. K. Cooper, S. Gul, F. M. Toma, L. Chen, Y.-S. Liu, J. Guo, J. W. Ager, J. Yano, I. D. Sharp, *J. Phys. Chem. C* **2015**, *119*, 2969–2974.

[57] P. S. Shinde, A. Annamalai, J. Y. Kim, S. H. Choi, J. S. Lee, J. S. Jang, *J. Phys. Chem. C* **2015**, *119*, 5281–5292.

[58] S. Sarkar, V. Gupta, M. Kumar, J. Schubert, P. T. Probst, J. Joseph, T. A. F. K"onig, *ACS Appl. Mater. Interfaces* **2019**, *11*, 13752–13760.

[59] S. Byun, B. Kim, S. Jeon, B. Shin, *J. Mater. Chem. A* **2017**, *5*, 6905–6913.

[60] F. F. Abdi, T. J. Savenije, M. M. May, B. Dam, R. van de Krol, *J. Phys. Chem. Lett.* **2013**, *4*, 2752–2757.

[61] M. Li, L. Zhao, L. Guo, *Int. J. Hydrogen Energy* **2010**, *35*, 7127–7133.

# RESEARCH ARTICLES

**Metal oxide semiconductors**, such as hematite or bismuth vanadate, can be used as photoanodes in devices using sunlight to transform water into dihydrogen. In this work, we present an innovative strategy to enhance their performances. High refractive index nanoparticles such as $TiO_2$ deposited on the surface enable to increase the amount of light absorbed in the active layer.
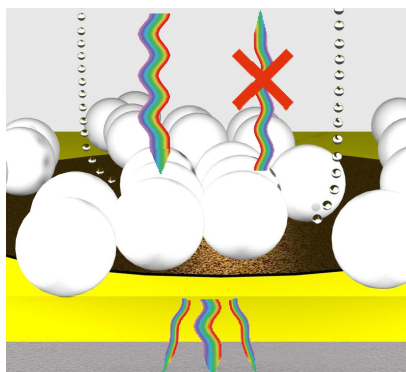
*L. Driencourt, Dr. B. Gallinet\*,*
*Prof. Dr. C. E. Housecroft, Dr. S. Fricke,*
*Prof. Dr. E. C. Constable\**

**High Refractive Index Dielectric Nanoparticles for Optically-Enhanced Activity of Water-Splitting Photoanodes**